World Electric Vehicle Journal

MDPI

Article

Comparative Analysis of Parallel Hybrid Magnet Memory Machines with Different PM Arrangements

Yixian Wang, Hui Yang *, Hao Zheng, Heyun Lin and Shukang Lyu

School of Electrical Engineering, Southeast University, Nanjing 210000, China; seueelab_wyx@163.com (Y.W.); seueelab_zh@163.com (H.Z.); hyling@seu.edu.cn (H.L.); seueelab_lsk@163.com (S.L.)
* Correspondence: huiyang@seu.edu.cn; Tel.: +86-15251867159

Abstract: This paper presents a comparative analysis of two parallel hybrid magnet memory machines (PHMMMs) with different permanent magnet (PM) arrangements. The proposed machines are both geometrically characterized by a parallel U-shaped hybrid PM configuration and several q-axis magnetic barriers. The configurations and operating principles of the investigated machines are introduced firstly. The effect of magnet arrangements on the performance of the proposed machines is then evaluated with a simplified magnetic circuit model. Furthermore, the electromagnetic characteristics of the proposed machines are investigated and compared by the finite-element method (FEM). The experiments on one prototype are carried out to validate the FEM results.

Keywords: hybrid magnet; memory machine; parallel magnetic circuit; permanent machine; variable flux

Citation: Wang, Y.; Yang, H.; Zheng, H.; Lin, H.; Lyu, S. Comparative Analysis of Parallel Hybrid Magnet Memory Machines with Different PM Arrangements. *World Electr. Veh. J.* **2021**, *12*, 177. https://doi.org/10.3390/wevj12040177

Academic Editors: C. C. Chan, Yoichi Hori, James L. Kirtley, Jr., Joeri Van Mierlo, Myoungho Sunwoo and Xuhui Wen

Received: 21 August 2021
Accepted: 28 September 2021
Published: 3 October 2021

1. Introduction

Recently, permanent magnet (PM) machines have been widely used in electric vehicle (EV) applications due to their high power density and efficiency [1,2]. The basic characteristics which are required for a traction machine mainly include the following:

(1) High torque density and power density; high torque for starting, at low speeds and hill climbing, and high power for high-speed cruising;
(2) wide speed range, with a constant power operating range of around 3~4 times the base speed being a good compromise between the peak torque requirement of the machine and the volt-ampere rating of the inverter;
(3) high efficiency over wide speeds and torque ranges, including low torque operation;
(4) intermittent overload capability, typically twice the rated torque for short durations;
(5) high reliability and robustness appropriate to the vehicle environment;
(6) acceptable cost;
(7) low acoustic noise and low torque ripple.

The most important design requirements of traction machines for electric vehicles are to achieve rated operating conditions (torque) and maximum operating range (maximum speed). Therefore, the air gap magnetic field of the motor needs to be adjusted. However, owing to the high coercive force of rare-earth PM, it is difficult to adjust the PM field to obtain a wide constant power speed range [1]. In order to achieve a flexible air-gap flux adjustment, d-axis flux-weakening (FW) current is normally applied [2]. Nevertheless, the FW current increases the potentially irreversible demagnetization risk of PM. Meanwhile, the resultant FW excitation copper loss reduces the operating efficiency particularly under high-speed conditions [1].

Variable flux memory machine (VFMM) has been considered as an effective solution to resolve the conflict between high torque at low-speed conditions and constant power maintaining capability at high-speed conditions in conventional PM machines [3–19]. The low coercive force (LCF) magnet in VFMM makes air-gap flux regulation convenient by applying a temporary magnetizing or demagnetizing current pulse [3,4]. Meanwhile, there

is a negligible associated excitation loss during the flux regulation, which achieves excellent FW capability and high efficiency over a wide speed range. Nonetheless, due to the low torque density of VFMMs having the LCF magnet as the only magnetomotive force (MMF) source, some hybrid PM VFMMs were presented and extensively investigated [5–15].

By considering the magnetic circuit relationship between NdFeB and LCF magnets, hybrid PM VFMMs can be generally divided into series [8–11] and parallel structures [11–15], respectively. For the series structures [8–11], the magnetization state (MS) of the LCF PM is not susceptible to the armature reaction demagnetization due to the stabilizing effect of the NdFeB magnet under on-load conditions. However, the NdFeB magnet is likely to cause a reverse magnetization of the LCF PM, which leads to a relatively limited air-gap flux adjustment range [8–11]. On the other hand, for the parallel hybrid magnet memory machine (PHMMM) [11–15], the two types of PMs are independent of each other, so that a flexible online flux regulation can be achieved. However, the LCF PM is susceptible to the on-load demagnetization caused by armature reaction or NdFeB PM field, thereby reducing the torque density [12,13]. For addressing this issue, the rotor can be improved by adding multiple q-axis magnetic barriers. This design can reduce the q-axis inductance and alleviate the cross-coupling effect [17–20]. Meanwhile, a positive d-axis current can be used to produce positive reluctance torque and prevent on-load magnet demagnetization [21].

However, in the previous studies of PHMMM, the impact of different PM arrangements on the electromagnetic performance remains unreported. Therefore, this paper aims to focus on this topic to provide some constructive design guidelines. This paper is organized as follows: in Section 2, the proposed machine topologies and features are described firstly. In addition, the operating principle is introduced based on the nonlinear hysteresis model of the LCF PM. Afterwards, the simplified magnetic circuits are established and modeled to analytically reveal the flux regulation principle in Section 3. Section 4 is devoted to a comparison of the electromagnetic characteristics of two PHMMMs with different PM arrangements. The experiments on a PHMMM are carried out to validate the finite-element method (FEM) results in Section 5, followed by a conclusion in Section 6.

2. Configurations and Operating Principle

2.1. Machine Configurations

Figure 1 shows the configurations of the PHMMMs with different PM arrangements. Both machines employ an identical stator structure featuring a 21-stator-slot/4-rotor-pole factional-slot distributed winding. For PM machine design, when the number of pole pairs p is small, the space of each pole in the proposed machine is larger, which is beneficial to expand the design space of the hybrid permanent magnet, as well as increase the flux regulation capability. On the other hand, the iron core saturation is smaller in the case of lower rotor pole number, which is also advantageous to the reduction in iron loss. However, in the meantime, the pole arc coefficient of the machine is relatively large, resulting in large magnetic flux leakage. Therefore, the number of poles of $2p = 4$ is selected. In order to reduce high-order back-EMF harmonics and cogging torque, a fractional slot winding is used. Furthermore, in order to facilitate the comparison with the other similar prototypes in the research group, a 21-slot structure is adopted. According to the PM type located on the two sides or at bottom of the U-shaped structure within one rotor pole, the PHMMMs are divided into HCF-LCF-HCF (HLH) and LCF-HCF-LCF (LHL) structures, respectively. The magnetic fields generated by the HCF magnets are either enforced to the air gap or short-circuited as the LCF PMs are magnetized in either the same or opposite direction with the HCF PMs. Consequently, the air-gap flux density can be flexibly adjusted, as shown in Figure 2.

2.2. Operating Principle

The flux adjusting principle can be illustrated from the perspective of the simplified hysteresis model of LCF PMs. As shown in Figure 3, it is assumed that the main hysteresis

loop and all the minor loops have the same value of coercive force H_{c2}, but the values of remanence B_{r1k} are different. The set of recoil lines can be expressed as [14,15]:

$$B = \mu_0 \mu_r H_m + B_{r1k} \tag{1}$$

where μ_0 and μ_r are the vacuum permeability and the relative permeability of LCF PMs, respectively; H_m is the remagnetizing field intensity, while B_{r1k} represents the remanence corresponding to the kth sets of hysteresis loops.

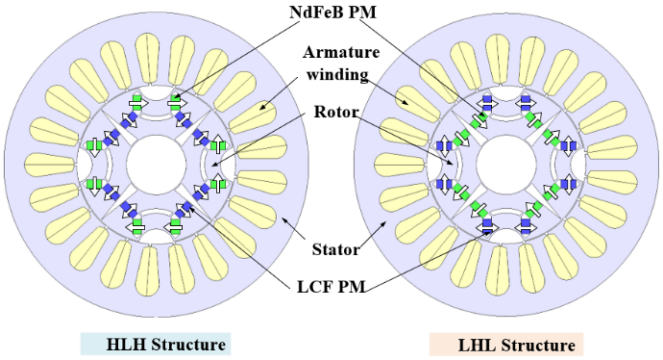

Figure 1. PHMMM configurations.

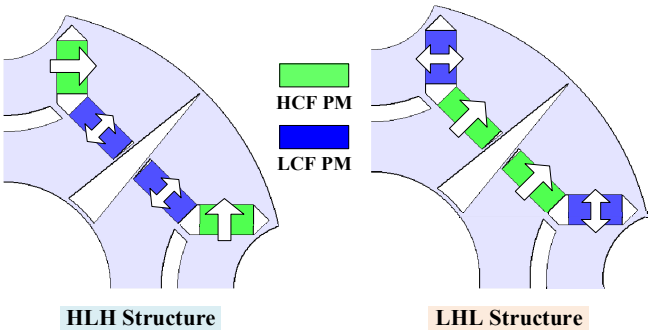

Figure 2. Schematic of proposed two different PM arrangements structures.

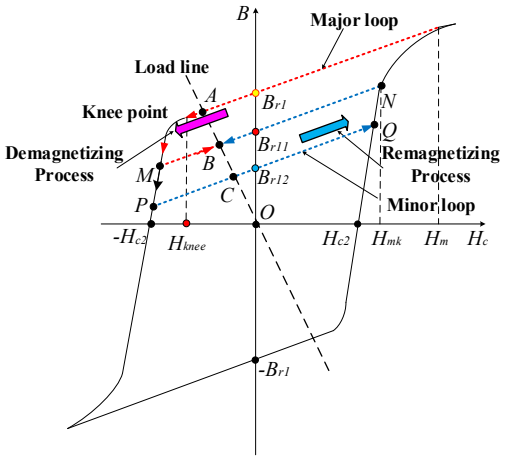

Figure 3. Simplified hysteresis model of the LCF PMs.

In order to compare the electromagnetic performance of the machines at different MSs, a magnetization ratio k_{mr} of the LCF PM can be defined as a ratio of B_{r1k} to the remanence B_{r1}, i.e.,

$$k_{mr} = \frac{B_{r1k}}{B_{r1}}, \quad n = 1, 2, 3 \ldots \tag{2}$$

In general, the magnetization ratio k_{mr} ranges from -1 to 1, which means that the flux linkage can be flexibly adjusted as the operating point of LCF PM moves along the different recoil lines. The value of k_{mr} is "1" when the LCF PMs are magnetized with HCF PMs in the same direction, while changes to "-1" with two opposite magnetized directions in turn. Figure 4 shows the open-circuit field distributions of the HLH and LHL structure under the flux-enhanced (K_{mr} = 1) and flux-weakened (K_{mr} = -1) states. It is clear to see that the magnetic flux paths and flux density distributions of the two structures are basically the same under the flux-enhanced state. On the other hand, the HCF PM fields are short-circuited by the LCF PM fields at the flux-weakened state, leading to a flux loop formed within the rotor core.

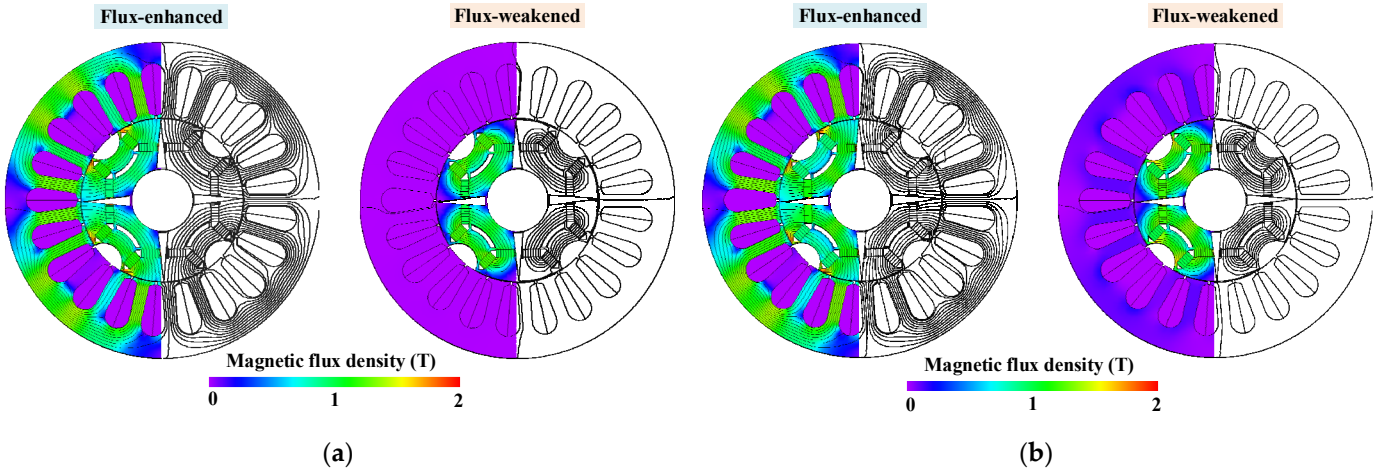

Figure 4. Open-circuit field distributions of proposed PHMMMs under different magnetization. (**a**) HLH structure. (**b**) LHL structure.

3. Analytical Analyses of PHMMM

In order to qualitatively reflect the possible effects of the PM arrangements on the flux adjusting range, a simplified equivalent magnetic circuit of PHMMM is established as shown in Figure 5. The peak air-gap fluxes at the flux-enhanced/weakened states are expressed as [7].

$$\Phi_{\delta+} = \frac{F_{m1}R_{m2} + F_{m2}R_{m1}}{R_g(R_{m1} + R_{m2}) + R_{m1}R_{m2}} \tag{3}$$

$$\Phi_{\delta-} = \frac{F_{m1}R_{m2} - F_{m2}R_{m1}}{R_g(R_{m1} + R_{m2}) + R_{m1}R_{m2}} \tag{4}$$

where F_{m1} and F_{m2} represent the equivalent MMFs of HCF and LCF PMs, respectively. Besides, R_{m1} and R_{m2} are the magnetic reluctances of HCF and LCF PMs, respectively, while R_g is the air-gap magnetic reluctance.

Moreover, the flux adjusting ratio α_m can be expressed as:

$$\alpha_m = \Phi_{\delta+}/\Phi_{\delta-} \tag{5}$$

Therefore, by substituting $\Phi_{\delta+}$ and $\Phi_{\delta-}$ into (5), the flux adjusting ratio of the proposed HPMMM can be rewritten as:

$$\alpha_m = 1 + \frac{2F_{m2}R_{m1}}{F_{m1}R_{m2} - F_{m2}R_{m1}} \tag{6}$$

Further simplifying the above formula:

$$\alpha_m = \frac{H_{c1}\mu_{r1}A_{m1} + H_{c2}\mu_{r2}A_{m2}}{H_{c1}\mu_{r1}A_{m1} - H_{c2}\mu_{r2}A_{m2}} = \frac{\frac{H_{c1}\mu_{r1}A_{m1}}{H_{c2}\mu_{r2}A_{m2}} + 1}{\frac{H_{c1}\mu_{r1}A_{m1}}{H_{c2}\mu_{r2}A_{m2}} - 1} \tag{7}$$

where H_{c1} and H_{c2} are the coercive forces of LCF and HCF PMs, respectively; μ_{r1} and μ_{r2} are the relative permeability of LCF and HCF PMs, respectively; moreover, A_{m1} and A_{m2} represent the cross-sectional, respectively.

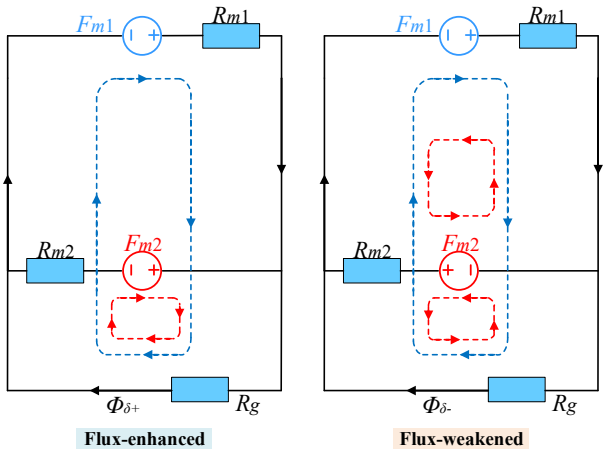

Figure 5. Simplified equivalent magnetic circuit of proposed PHMMM.

Therefore, it can be seen that the flux adjusting ratio α_m of the PHMMM is associated with the ratio of A_{m1} to A_{m2}. Since the level of the coercive force and remanence of the two types of PMs are different, even if the usage of two kinds of PMs in different structures is the same, the thickness of the two types of PMs is still different due to the geometric limitation of the U-shaped structure, so that the magnetic resistances of the two types of PMs in HLH and LHL structures are unequal. As a result, the peak air-gap fluxes of the HLH and LHL structures are different.

After comparing the cross-sectional areas of LCF and HCF PMs in HLH and LHL structures, the HLH structure owing a wider flux adjusting range on account of the larger ratio of A_{m1} to A_{m2}, which can be also evidenced by the open-circuit field distributions in Figure 5. Moreover, the fundamental back EMFs, as functions of the magnetization ratio of LCF PMs, are shown in Figure 6. It can be observed that the HLH structure shows a slightly wider flux regulation range due to the larger ratio of A_{m1} to A_{m2}, as presented in (7). In addition, the HLH structure shows quite a low fundamental back EMF at the flux-weakened state, resulting in low torque and efficiency. In this case, according to the required flux adjusting range of three times, the MSs "$K_{mr} = 1$" and "$K_{mr} = -0.5$" are chosen for further analysis.

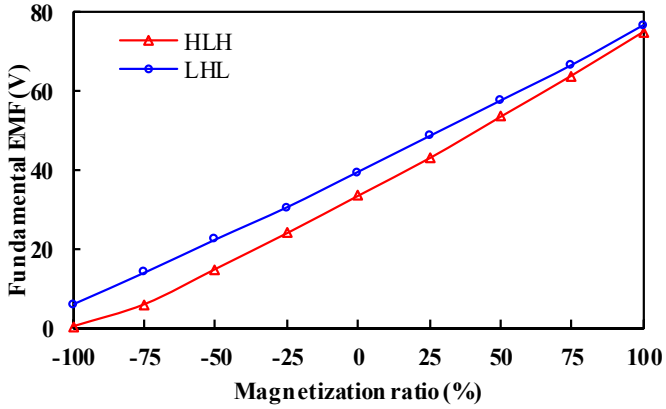

Figure 6. Variation of back EMF fundamental magnitude with the magnetization ratio of LCF PMs.

4. Electromagnetic Performance Comparison

The electromagnetic characteristics of the proposed PHMMM with HLH and LHL structures are compared in this Section. The design parameters of the two structures are listed in Table 1. It should be noted that the two structures share the same stator, HCF and LCF magnet usage, overall dimensions, as well as electric loading in order to ensure the fairness of the comparison.

Table 1. Key design parameters of proposed PHMMMs.

Items	HLH	LHL
Rated power (kW)	1.2	
Rated speed (r/min)	1500	
Outer diameter of stator (mm)	122	
Inner diameter of stator (mm)	63.5	
Back-iron thickness (mm)	8.25	
Stator tooth width (mm)	4.8	
Air-gap length (mm)	0.35	
Active stack length (mm)	55	
HCF PM grade	NdFeB	N35SH
LCF PM grade	AlNiCo 9	
HCF/LCF PM coercivity (kA/m)	915/112	
HCF/LCF PM remanence (T)	1.2/1.0	
Steel grade	35CS440	
HCF PM thickness × length (mm × mm)	3.5 × 6	3 × 7
LCF PM thickness × length (mm × mm)	3 × 7	3.5 × 6
Armature winding turns per phase	210	
Rated current (Arms)	6.35	
Current density (A/mm2)	6.5	
DC-link voltage U_{dc} (V)	200	

4.1. Open-Circuit Performance

The open-circuit back EMFs and harmonic spectra of the two PHMMMs under different MSs are shown in Figure 7. It can be seen that the LHL structure shows higher EMF magnitude at both two different MSs.

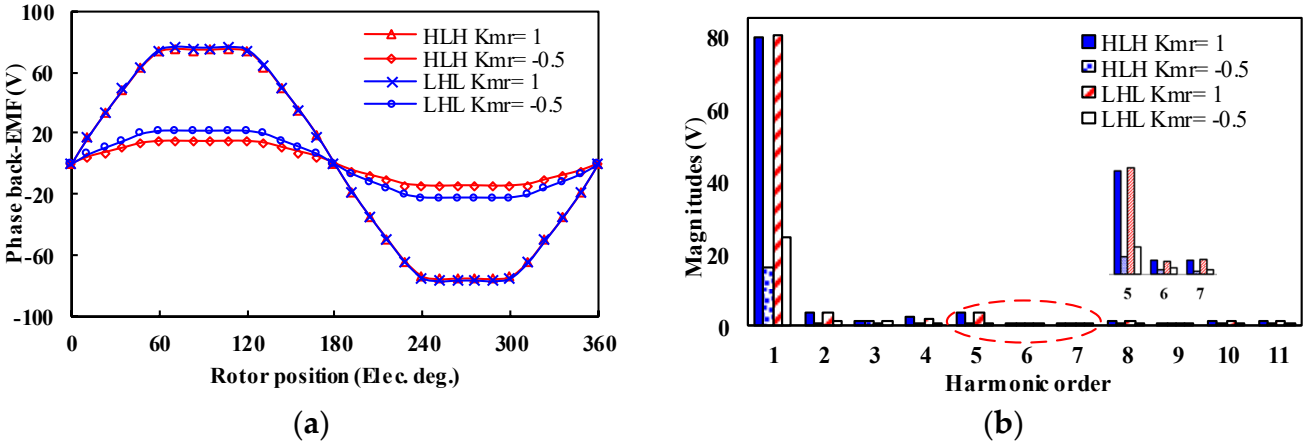

Figure 7. Back EMF waveforms. (**a**) Waveforms. (**b**) Harmonic spectra.

The corresponding air-gap flux density waveforms and harmonic spectra under different MSs are shown in Figure 8. The LHL structure shows a higher magnitude of flux density under $K_{mr} = -0.5$ state, while the flux density of the LHL structure under $K_{mr} = 1$ state is basically the same as the HLH structure.

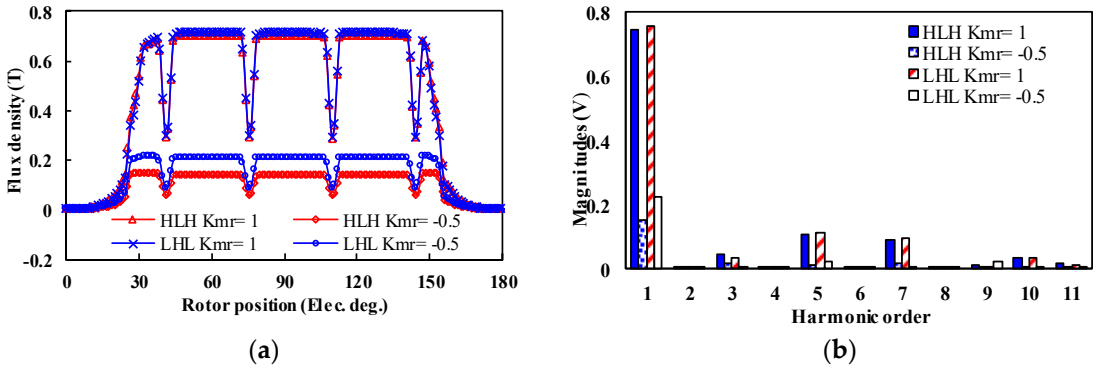

Figure 8. Open-circuit air gap flux density waveforms under different MSs. (**a**) Waveforms. (**b**) Harmonic spectra.

4.2. Magnetization Performance

The working point variations of the two PHMMMs before and after applying one electrical period of a *d*-axis demagnetizing current pulse of 2A are shown in Figure 9. The HLH structure is more susceptible to be demagnetized since the LCF PMs in the HLH structure are located closer to the *d*-axis centerlines.

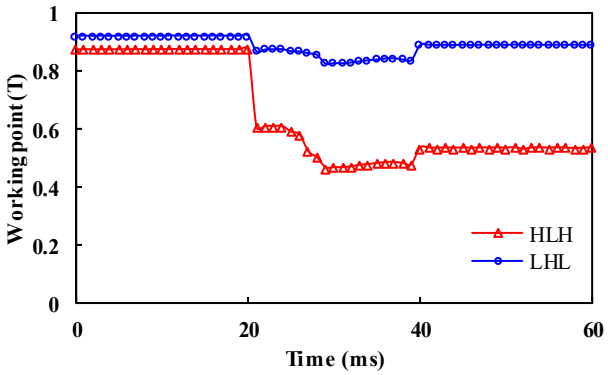

Figure 9. Variations of LCF PM working point of HLH and LHL structures subject to a *d*-axis demagnetizing current pulse of 2A.

Figures 10 and 11 show the variation of fundamental EMF with the applied *d*-axis demagnetizing and remagnetizing current pulse, respectively. The HLH structure requires smaller demagnetizing and remagnetizing current amplitudes. It indicates that the inverter rating of the HLH structure is lower than that of the LHL case, which is beneficial for cost-effective applications.

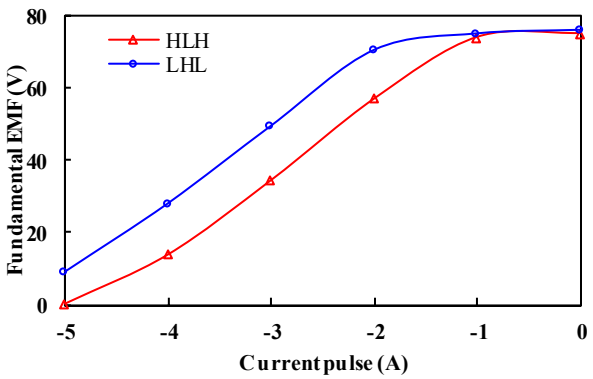

Figure 10. Open-circuit back-EMF fundamental magnitudes of two structures as functions of demagnetizing current pulse @ 1500 r/min.

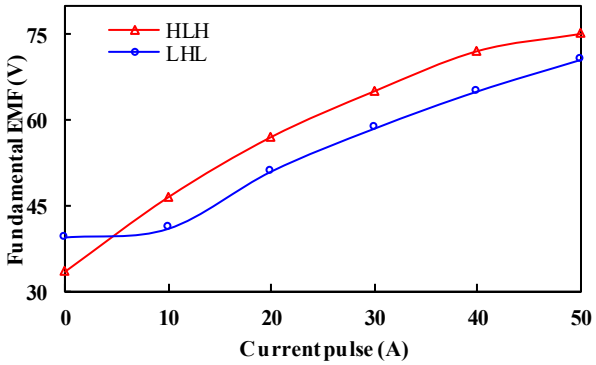

Figure 11. Open-circuit back-EMF fundamental magnitudes of two structures as functions of remagnetizing current pulse @ 1500 r/min.

4.3. Torque Characteristics

The inductance characteristics of the machine not only affect the flux regulation range but also have an effect on torque capability. For the proposed PHMMMs, the d/q-axis inductance curves of two types of structures under different current angles are shown in Figure 12. It should be noted that the current angle is defined as based on the q axis, which is used to express the phase relationship between the EMF E_0 and the armature current I_a, that is to say, q axis refers to the current angle of 0 current degrees, and d axis corresponds to the current angle of -90 current degrees. It is obvious that the d-axis inductance experiences a more significant fluctuation than the q-axis inductance for the two structures due to the design of the q-axis barriers. For the HLH structure, the flux-intensifying characteristics with "$L_d > L_q$" can be achieved when the current angle is between "-15" and "35" degrees. For the LHL structure, the range will be slightly reduced, between"-5" and "35" degrees.

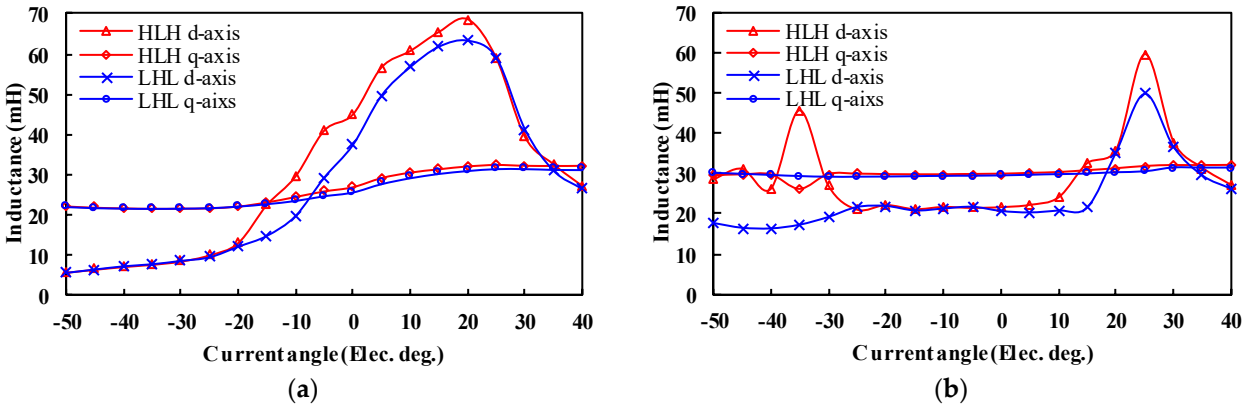

Figure 12. Comparison of d/q-axis inductance in two structures under various current angles. (**a**) Kmr = 1. (**b**) Kmr = -0.5.

The cogging torque curves under different MSs are shown in Figure 13. It can be seen that the ripple patterns of the cogging torque of the two cases under the "$K_{mr} = 1$" state are basically the same. However, the LHL structure torque amplitude is relatively higher under the "$K_{mr} = -0.5$" state. This is mainly resulted from larger fifth-order harmonics in the back EMFs, as reflected in Figure 7b.

The torque against current angle characteristics under the flux-enhanced state is illustrated in Figure 14. It can be observed that the maximum torques all occur at a negative current angle of -10 and -5 electrical degrees for the HLH and LHL structures, respectively. Furthermore, the reluctance torque is positive in the selected current angle range, which increases the total torque capability.

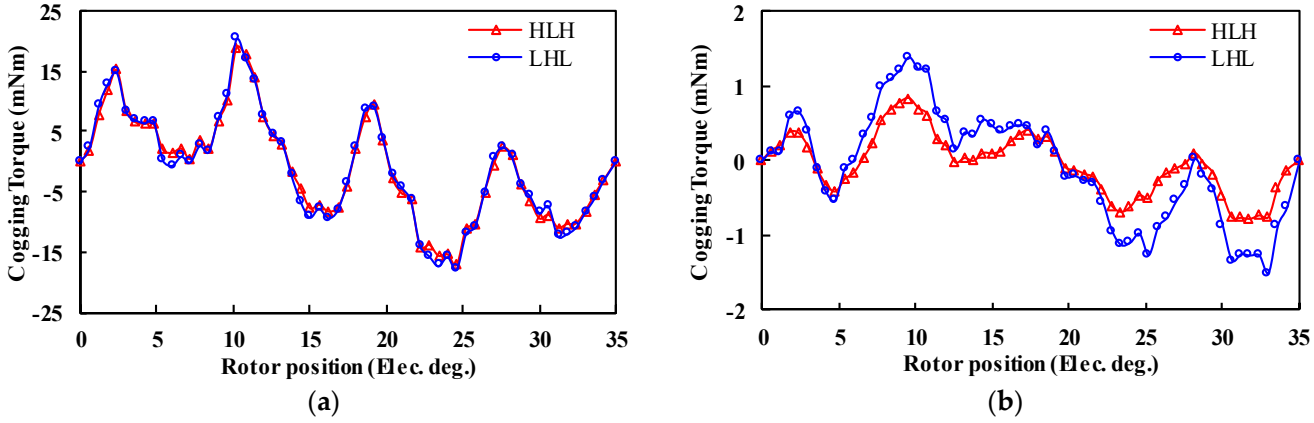

Figure 13. Cogging torque of HLH and LHL structures under different MSs. (**a**) K_{mr} = 1. (**b**) K_{mr} = −0.5.

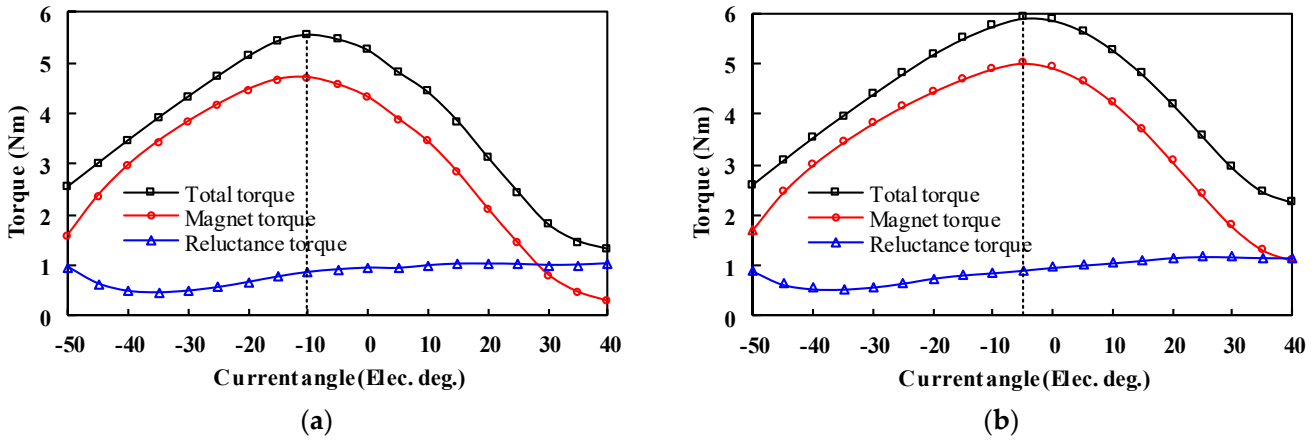

Figure 14. Torque against current angle characteristics (rated current = 6.35 Arms) when K_{mr} = 1. (**a**) HLH structure. (**b**) LHL structure.

The torque against current angle characteristics under the "K_{mr} = −0.5" state is illustrated in Figure 15. It can be observed that the maximum torques all occur at a positive current angle of 15 and 25 elec. deg. in the two cases, respectively. Due to the low MS of the LCF PMs, the magnet torque decreases significantly compared with that at the flux-enhanced state.

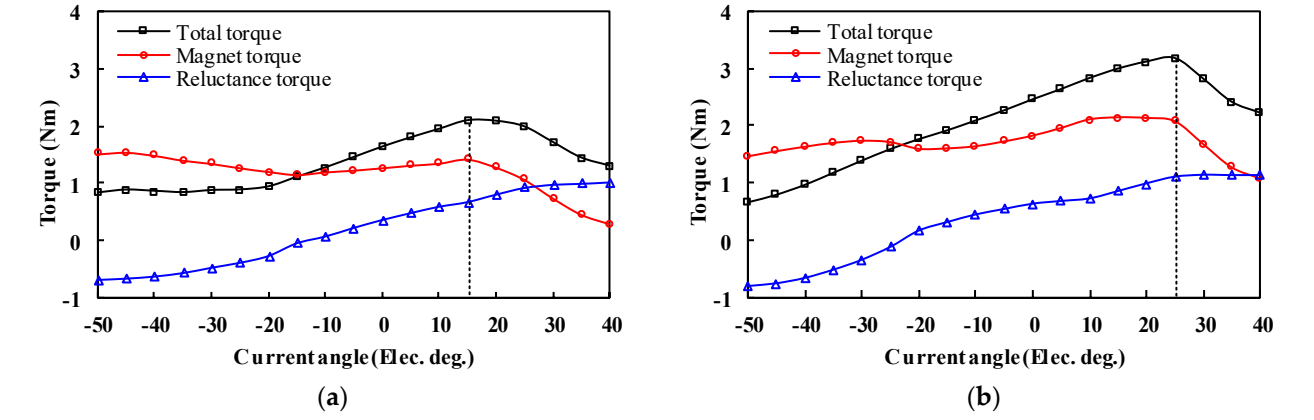

Figure 15. Torque against current angle characteristics (rated current = 6.35 Arms) when K_{mr} = −0.5. (**a**) HLH structure. (**b**) LHL structure.

Furthermore, the steady torque waveforms under the maximum torque-per-ampere (MTPA) control with rated current density are shown in Figure 16. It implies that the LHL structure exhibits higher torque and less torque ripple rate than the HLH counterpart regardless of MS.

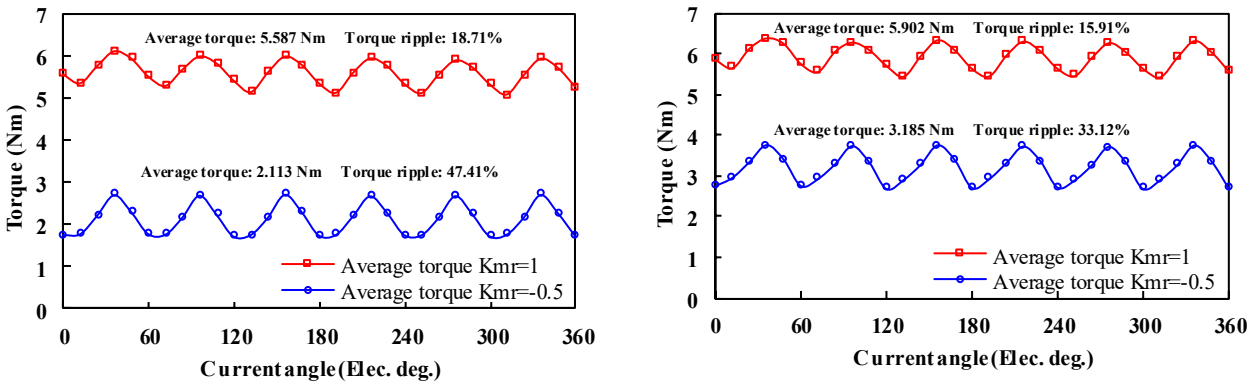

Figure 16. Steady torque waveforms (rated current = 6.35 Arms). (**a**) HLH structure. (**b**) LHL structure.

4.4. Demagnetization Withstand Capability

The unintentional cross-coupling demagnetization caused by the armature reaction or NdFeB PM field in two PHMMMs should be further examined.

The cross-coupling demagnetization ratio can be defined as [7,14]:

$$DR = (E_1 - E_2)/E_1 \times 100\% \quad (8)$$

where E_1 and E_2 are the fundamental back EMFs before and after applying rated current. The demagnetization ratio DR of the two structures under different loads is calculated, as shown in Figure 17.

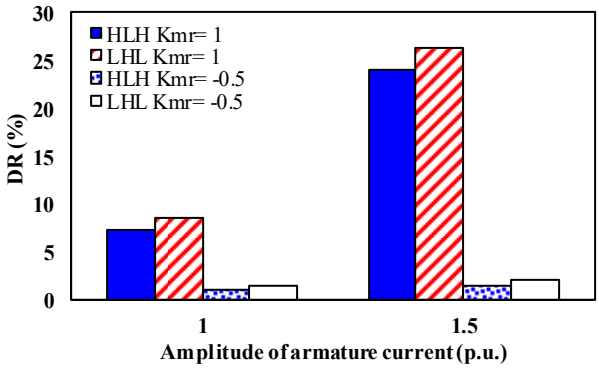

Figure 17. Comparison of demagnetization ratios under different armature currents.

The demagnetization ratios of the LHL structure under different armature currents when K_{mr} = 1 are higher than those of the HLH structure. Moreover, the unintentional demagnetization will aggravate with larger current amplitude. In addition, both two structures show a small cross-coupling demagnetization ratio under the "$K_{mr} = -0.5$" state. This is because the HCF PMs are short-circuited by LCF PMs, leading to a flux loop formed within the rotor core. In this case, the HCF PMs can stabilize the working points of the LCF PMs in turn. It can be summarized that the LHL structure turns out to be more susceptible to the armature reaction, which shows a lower undesired demagnetization withstand capability.

4.5. Efficiency Performance

The five commonly used magnetization states (K_{mr} = ±1, ±0.5, 0) of the two motors are simulated, and the comprehensive efficiency map is obtained as shown in Figure 18. It can be seen that both motors have relatively high comprehensive efficiency.

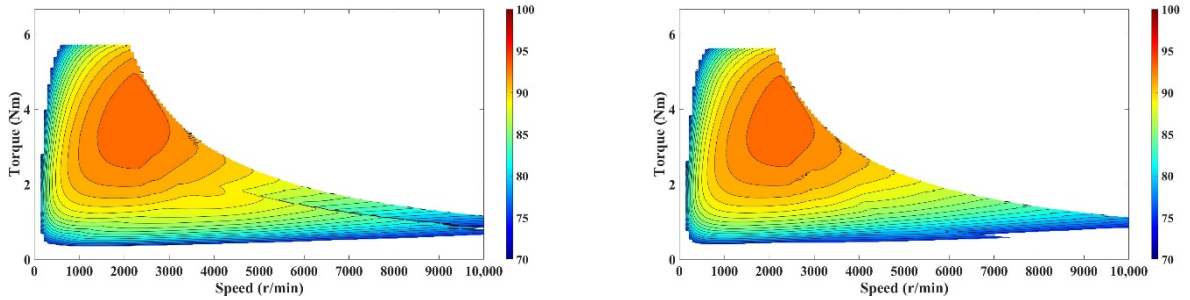

Figure 18. Comparison of overall efficiency. (**a**) HLH structure. (**b**) LHL structure.

5. Experimental Verification

In order to validate the proceeding analyses, an HLH PHMMM is manufactured and tested. The fabricated machine is shown in Figure 19. Figure 20 is a schematic diagram of the test platform. The test platform basically includes an adjustable DC power supply, inverter, PC, test prototype, coupling, load machine, and controller. The adjustable DC power supply injects a three-phase current into the inverter to drive the PHMMM for motoring operation. In addition, the PC terminal can use the controller to apply instantaneous *d*-axis current pulses to change the MS during the load operation. The prototype drives the load machine to rotate at the same speed through the coupling. At this time, the torque data can be fed back to the PC in real time through the torque sensor to record the relevant data. The actual test platform is shown in Figure 21.

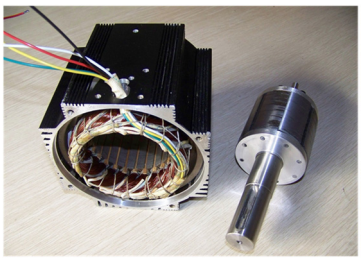

Figure 19. Manufactured prototypes of the HLH PHMMM.

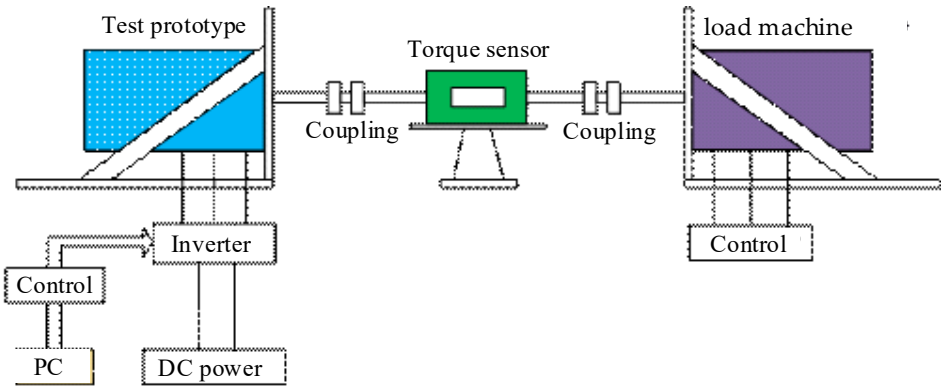

Figure 20. Schematic diagram of the test platform.

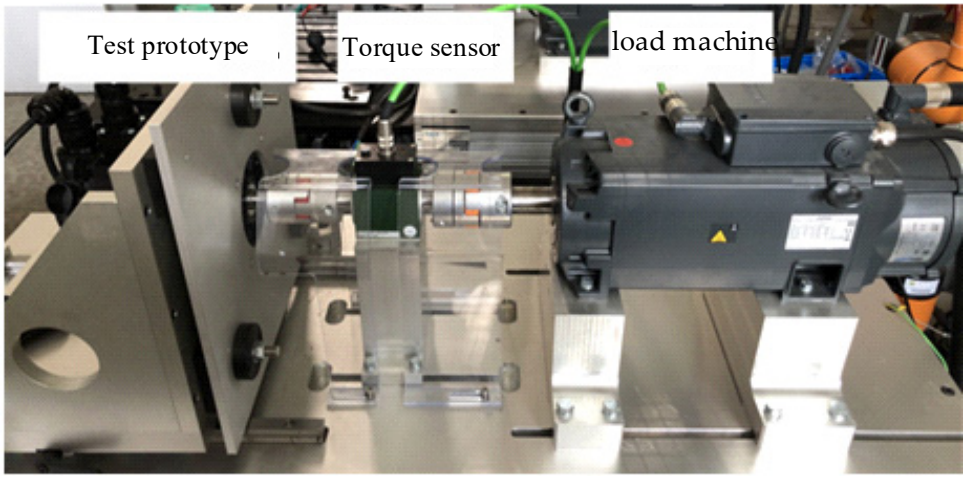

Figure 21. Actual diagram of the control circuit of the test platform.

In the finite element simulation, the flux regulation ability is normally reflected by the air-gap flux density. However, in the actual testing process, since the motor's air-gap flux density cannot be measured directly, it is usually characterized by the no-load back EMF amplitude of the machine under different MSs. Figure 22 shows the phase fundamental EMF of the manufactured PHMMM with the applied d-axis demagnetizing and remagnetizing current pulses that have been measured and compared with FE-predicted ones. As expected, the 2D-FEM results are consistent with the experimental results. It can be observed that the HLH PHMMM shows a wide flux adjusting range, which confirms the foregoing FEM analyses.

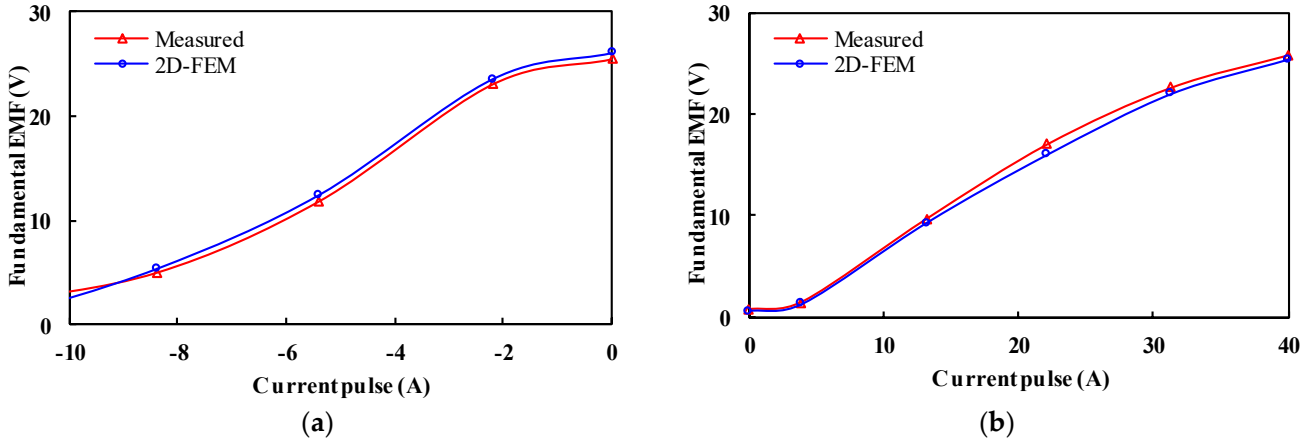

Figure 22. Comparison of the back-EMF fundamental magnitudes as functions of (**a**) demagnetizing and (**b**) remagnetizing current pulse.

Similar to the simulation process, the experiment was also carried out in two magnetization states, namely the high magnetization state $K_{mr} = 1$ and the low magnetization state $K_{mr} = -0.5$. The torque-speed curves obtained are shown in Figure 23, and the experimental results can be seen to have high consistency with the simulation.

Figure 24 shows the measured torque-speed curves in $K_{mr} = 1$ and $K_{mr} = -0.5$ states. It can be seen that it is similar to the simulation situation. The pulse current demagnetization can be applied to the motor at point A to effectively broaden the motor operating area. The turning speed is about 3200 rpm.

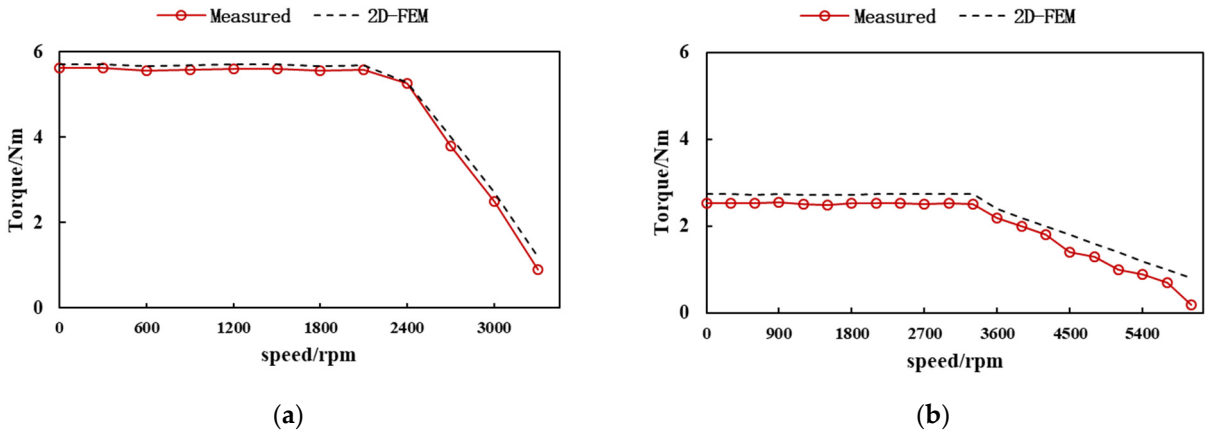

Figure 23. The T-N curve of PHMMM under the control of i_d constant 0. (**a**) K_{mr} = 1 (**b**) K_{mr} = −0.5.

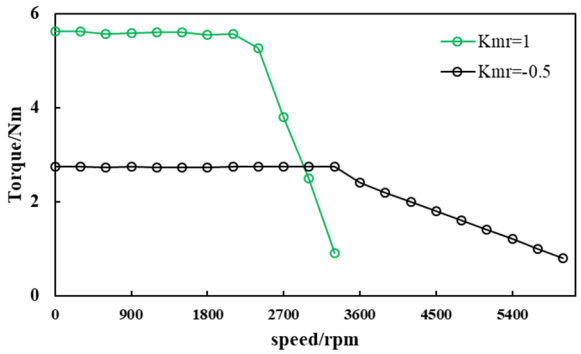

Figure 24. The measured T-N curve of VFMM under the control of i_d constant 0.

6. Conclusions

This paper presents a comparative study of the PHMMMs with different PM arrangements. According to the arrangement of the two types of magnets, the PHMMMs can be divided into HLH and LHL structures. The simplified magnetic circuit models of the PHMMMs under different MSs are analyzed, it can be deduced that the HLH structure can obtain a relatively wider flux regulation range. Further, the electromagnetic characteristics of the proposed PHMMM with different PM arrangements are comprehensively compared. It is found that the LHL structure exhibits higher torque density and lower torque ripple than the HLH structure due to its higher peak air-gap flux density and less high-order harmonics. On the other hand, better demagnetization withstands capability, lower magnetizing current, and inverter rating can be observed in the HLH structure. Finally, a PHMMM with an HLH structure is fabricated and tested, which confirms that the HLH structure can achieve a wide flux regulation range. Overall, both PHMMMs have their own merit and demerit and should be selected according to the requirements for the specific applications.

Author Contributions: Conceptualization, Y.W. and H.Y.; methodology, H.Y.; software, H.Z.; validation, H.Z. and S.L.; formal analysis, Y.W.; investigation, S.L.; resources, Y.W. and H.Y.; data curation, H.Z.; writing—original draft preparation, Y.W. and H.Z.; writing—review and editing, H.Y. and H.L.; visualization, Y.W.; supervision, H.Y.; project administration, H.Y.; funding acquisition, H.Y. All authors have read and agreed to the published version of the manuscript.

Funding: This work was jointly supported in part by National Natural Science Foundations of China under Grants (52077033 and 52037002), in part by Key R&D Program of Jiangsu Province (BE2021052), in part by the Fundamental Research Funds for the Central Universities (2242017K41003), in part by Supported by the "Zhishan Youth Scholar" Program of Southeast University, in part the Jiangsu Provincial Key Laboratory of Smart Grid Technology and Equipment, Southeast University (7716008046), and in part by supported by “the Excellence Project Funds of Southeast University”.

Conflicts of Interest: The authors declare no conflict of interest.

References

1. Zhu, Z.Q.; Howe, D. Electrical machines and drives for electric, hybrid, and fuel cell vehicles. *Proc. IEEE* **2007**, *95*, 746–765. [CrossRef]
2. Boldea; Tutelea, L.N.; Parsa, L.; Dorrell, D. Automotive electric propulsion systems with reduced or no permanent magnets: An overview. *IEEE Trans. Ind. Electron.* **2014**, *61*, 5696–5711. [CrossRef]
3. Ostovic, V. Memory motors. *IEEE Ind. Appl. Mag.* **2003**, *9*, 52–61. [CrossRef]
4. Yang, H.; Lin, H.; Zhu, Z.Q. Recent advances in variable flux memory machines for traction applications: A review. *CES Trans. Electr. Mach. Syst.* **2018**, *2*, 34–50. [CrossRef]
5. Sakai, K.; Yuki, K.; Hashiba, Y.; Takahashi, N.; Yasui, K. Principle of the variable-magnetic-force memory motor. In Proceedings of the International Conference on Electrical Machines and Systems, Tokyo, Japan, 15–18 November 2009; pp. 1–6.
6. Ibrahim, M.; Masisi, L.; Pillay, P. Design of variable-flux permanent magnet machines using Alnico magnets. *IEEE Trans. Ind. Appl.* **2015**, *51*, 4482–4491. [CrossRef]
7. Yang, H.; Zhu, Z.Q.; Lin, H.; Lyu, S. Comparative study of hybrid PM memory machines having single- and dual-stator configurations. *IEEE Trans. Ind. Electron.* **2018**, *65*, 9168–9178. [CrossRef]
8. Athavale, A.; Sasaki, K.; Gagas, B.S.; Kato, T.; Lorenz, R.D. Variable flux permanent magnet synchronous machine (VF-PMSM) design methodologies to meet electric vehicle traction requirements with reduced losses. *IEEE Trans. Ind. Appl.* **2017**, *53*, 4318–4326. [CrossRef]
9. Zhu, Z.Q.; Hua, H.; Pride, A.; Deodhar, R.; Sasaki, T. Analysis and reduction of unipolar leakage flux in series hybrid permanent-magnet variable flux memory machines. *IEEE Trans. Magn.* **2017**, *53*. [CrossRef]
10. Hua, H.; Zhu, Z.Q.; Pride, A.; Deodhar, R.P.; Sasaki, T. A novel variable flux memory machine with series hybrid magnets. *IEEE Trans. Ind. Appl.* **2017**, *53*, 4396–4405. [CrossRef]
11. Hua, H.; Zhu, Z.Q.; Pride, A.; Deodhar, R.; Sasaki, T. Comparative study of variable flux memory machines with parallel and series hybrid magnets. In Proceedings of the 2017 IEEE Energy Conversion Congress and Exposition (ECCE), Cincinnati, OH, USA, 1–5 October 2017; pp. 3942–3949.
12. Zhou, Y.; Chen, Y.; Shen, J.X. Analysis and improvement of a hybrid permanent-magnet memory motor. *IEEE Trans. Energy Convers.* **2016**, *31*, 915–923. [CrossRef]
13. Yang, H.; Zhu, Z.Q.; Lin, H.; Guo, K.; Guo, Y.; Fang, S.; Huang, Y. Analysis of on-load magnetization characteristics in a novel partitioned stator hybrid magnet memory machine. *IEEE Trans. Magn.* **2017**, *53*, 1–4. [CrossRef]
14. Yang, H.; Lin, H.; Zhu, Z.Q.; Wang, D.; Fang, S.; Huang, Y. A variable-flux hybrid-PM switched-flux memory machine for EV/HEV applications. *IEEE Trans. Ind. Appl.* **2014**, *52*, 2203–2214. [CrossRef]
15. Yang, H.; Zhu, Z.Q.; Lin, H.; Wu, D.; Hua, H.; Fang, S.; Huang, Y. Novel high-performance switched flux hybrid magnet memory machines with reduced rare-earth magnets. *IEEE Trans. Ind. Appl.* **2016**, *52*, 3901–3915. [CrossRef]
16. Wu, D.; Zhu, Z.Q.; Liu, X.; Pride, A.; Deodhar, R.; Sasaki, T. Cross coupling effect in hybrid magnet memory motor. In Proceedings of the 7th IET International Conference on Power Electronics, Machines and Drives (PEMD 2014), Manchester, UK, 8–10 April 2014; pp. 1–6.
17. Limsuwan, N.; Kato, T.; Akatsu, K.; Lorenz, R.D. Design and evaluation of a variable-flux flux-intensifying interior permanent-magnet machine. *IEEE Trans. Ind. Appl.* **2014**, *50*, 1015–1024. [CrossRef]
18. Kato, T.; Limsuwan, N.; Yu, C.; Akatsu, K.; Lorenz, R.D. Rare earth reduction using a novel variable magnetomotive force flux-intensified IPM machine. *IEEE Trans. Ind. Appl.* **2014**, *50*, 1748–1756. [CrossRef]
19. Fukushige, T.; Limsuwan, N.; Kato, T.; Akatsu, K.; Lorenz, R.D. Efficiency contours and loss minimization over a driving cycle of a variable flux-intensifying machine. *IEEE Trans. Ind. Appl.* **2015**, *51*, 2984–2989. [CrossRef]
20. Ibrahim, M.; Masisi, L.; Pillay, P. Design of variable flux permanent-magnet machine for reduced inverter rating. *IEEE Trans. Ind. Appl.* **2015**, *51*, 3666–3674. [CrossRef]
21. Chu, W.Q.; Zhu, Z.Q.; Zhang, J.; Liu, X.; Stone, D.A.; Foster, M.P. Investigation on operational envelops and efficiency maps of electrically excited machines for electrical vehicle applications. *IEEE Trans. Magn.* **2015**, *51*, 1–10. [CrossRef]